CHAPTER 1

Introduction: A bibliographic review

Chapter 1

1.1 Introduction

The present thesis is based upon the detail study of transport properties of some topological insulators (TIs) and Weyl semimetals (WSMs). In this chapter we have discussed some essential and important features of these materials. We have divided this chapter in two parts, which provides the brief introduction of TIs and WSMs. The unique properties of these materials prepare a good podium for understanding interesting physics and can potentially be used in future technological applications.

1.2 Topological Insulators

Topological insulators (TIs) have attracted immense interest of the research community for their unique physical properties and potential technological applications, such as in spintronic devices and quantum computing [1]–[3]. 3D topological insulator crystals host bulk band gap with gapless topological protected surface states (SS) by means of strong spin-orbit coupling (SOC) and preservation of time-reversal symmetry (TRS) [4]–[6]. The amalgamation of strong spin-orbit interaction and TRS makes surface states free from back scattering by crystal defects and non-magnetic impurities. Therefore, the electrical conduction is robust against backscattering on the surfaces of TIs. Besides this, TIs hold a π Berry phase because of spin-moment locking [3]. The realization of TIs has inaugurated a gush of research activities with anticipation of marvelous phenomena, including the quantum anomalous Hall effect (QAHE), possibility of neutral Majorana Fermions, topological superconductivity, novel magnetoelectric quantum states and magnetic monopole [1]–[3]. It has been observed that topological surface states (TSS) of a TI exhibit a linear energy-momentum (E-k) relation. Therefore, quantum magnetotransport phenomenon such as, Aharonov-Bohm oscillations, weak antilocalization effect and quantum conductance fluctuations are attributed to these TSS [6]. Moreover, large SOC

drives an inversion of the band at the gamma point near the Fermi level (E_F), which induces very interesting magnetotransport properties in these compounds.

In condensed matter physics the different phases of matter and transitions between them occur by change of temperature, pressure, and chemical potential. These transitions occur because of symmetry breaking as explained by Landau in his theory of phase transitions. In structural transitions the translational symmetry is broken, while in ferromagnets rotational symmetry is broken and in superconductors the gauge symmetry is broken. In 1980, Klaus von Klitzing et al. [7] introduced Integer Quantum Hall Effect (IQHE) state transition, the basic understating of phase transition could not explain the normal state to IQHE state transition on the basis of symmetry breaking alone. Thus, a new classification of phases was established by Thouless et al. [8] on the basis of topological properties of the ground state. If there is a change in the topological properties of the ground state, a system said to undergo the phase transition. To understand a topological phase transition we have to have an idea of topology.

1.3 Topology in Topological Phase

Topology is a mathematical term which classifies shape of object and deals with the properties of object which are invariant under smooth deformation, twisting and stretching. For example, two geometrical constructions that can be transformed into one another by smooth deformations are said to be topologically equivalent. The topological class is defined by the quantity called genus (g) in three dimensional Euclidean space. The genus is analogous to number of holes present in the geometry. Those geometries which contain the same number of holes are considered topologically equivalent. Therefore, a coffee mug and doughnut are topologically equivalent with g = 1, similarly a solid sphere and a solid cube are also topologically equivalent with g = 0. However, the solid sphere and the doughnut

are topologically non-equivalent as the solid sphere cannot be transformed into the doughnut without creating a hole in geometry but a coffee mug can be simply transformed into the shape of a doughnut. The topological equivalence between a coffee mug and a doughnut, sphere and a cube, and the non-equivalence between the doughnut and a sphere is shown in figure 1.1.

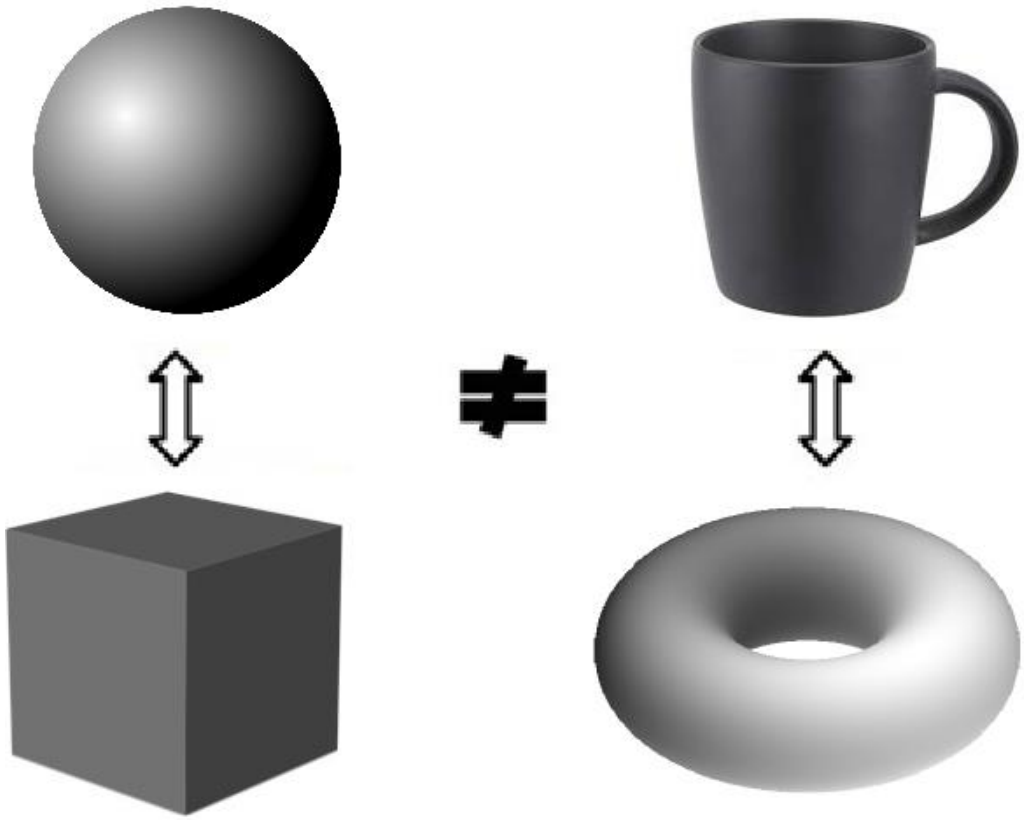

Figure 1.1: The sphere and cube on the left hand side are topologically equivalent and the coffee mug and the doughnut on the right are also topologically equivalent. The sphere and the coffee mug are topologically non-equivalent.

In other words, any two objects with the same value of genus can be smoothly transformed in one another without any change in their topological properties. The Gauss-Bonnet theorem connects the geometry (curvature) of objects to their topology and relates it to genus (g) of an object as,

$$\oint_{Surface}^{0} KdA = 4\pi(1-g) \quad (1.1)$$

Where *K* is the Gaussian curvature, g is the genus of the surface.

In a band insulator, such a 'smooth deformation' is similar to the modification in Hamiltonian of a many particle system, without shutting the bulk band gap. Two quantum states are said to be topologically equivalent only if a smooth transformation could take place from one state to the other without shutting the band gap. Hence, Insulators are topologically equivalent if they can be continuously transformed into one another without closing the energy gap [3].

1.4 Preservation of Time Reversal Symmetry (TRS)

Upon breaking of the symmetry we get interesting phase of matter by phase transition, i.e. liquid crystals are the examples of translation symmetry breaking phase, similarly superconductors are the examples of the gauge symmetry breaking phase of the matter. Contrastingly, beauty of topological insulator material is not due to breaking of symmetry but due to preservation of symmetry. The topological surface states (TSS) in TI always preserve time reversal symmetry (TRS). The TSS of TI are protected by TRS so they are robust against the nonmagnetic impurity or imperfection, hence, there is no backscattering of electron in these states. Due to large SOC and spin momentum locking, electron can move only in forward direction, they cannot move in backward direction without flipping there spin direction, because spin direction of the electron is uniquely tied to its momentum vector. Thus, there are two opposite paths for electron motion corresponding two opposite spins of electrons as shown in the figure 1.2.

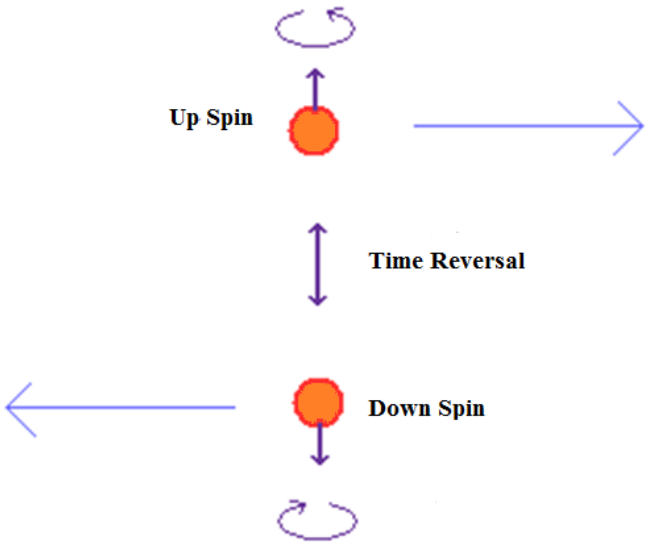

Figure 1.2: Schematic picture of electrons motion of two opposite spins with preservation of TRS in TSS.

1.5 Background of Topological Insulator

1.5.1 Hall Effect

The early seeds of topological insulator were laid down by Edwin Hall with the discovery of Hall effect in 1879 [9]. He measured a transfer voltage in a conducting bar perpendicular to the applied current; this voltage arises from the deflected motion of charged particles under external electric field and magnetic field. When magnetic field is applied in a direction normal to the applied electric current, the charge carriers experience a Lorentz force and accumulate on the opposite surfaces of the bar depending on their nature of charge. This effect is recognized as the Hall effect and the transfer voltage generated across the conductor is called as Hall voltage (V_H), the schematic diagram of Hall setup is shown in figure 1.3. By studying Hall effect, one can determine the nature of charge carriers (i.e. electrons or holes) as well as the density of carriers in the sample by following relations.

$$R_H = \frac{z\,V_H}{I_x B} = \frac{1}{ne} \tag{1.2}$$

Where, R_H is the Hall coefficient, I_x is current flows in plane of the conductor, z is the thickness of conducting bar, B is the applied magnetic field perpendicular to the plane of the bar ,V_H is the Hall voltage, n is the density of the charge carriers in the sample and e is the electric charge.

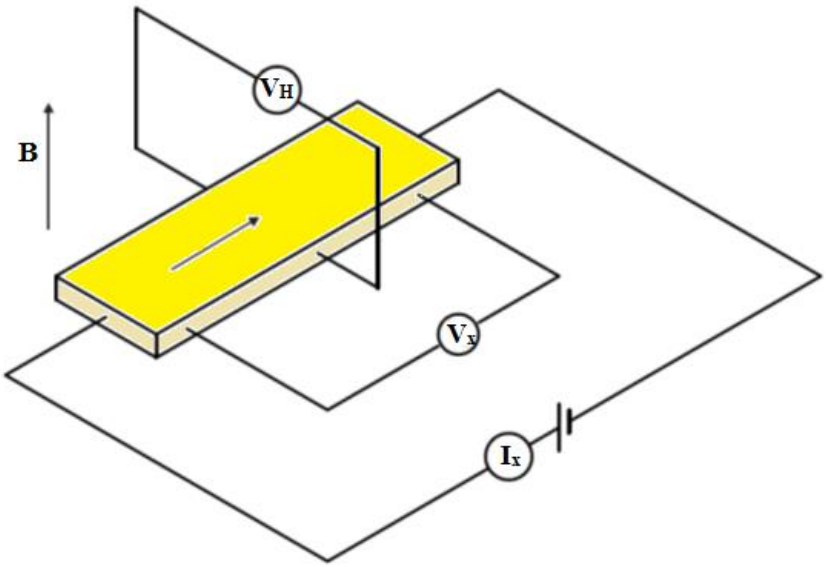

Figure 1.3: Electrical schematic of Hall effect geometry. The Current (I_x) flows in plane, perpendicular to an applied field B generating a Hall voltage V_H by action of the Lorentz force.

1.5.2 Integer Quantum Hall Effect (IQHE)

IQHE was observed by von Klitzing in 1980 [7] in two dimensional electron gas systems (2DEG) at very low temperature with the implementation of strong magnetic field. The quantization of the electrons motion in cyclotron orbits gives rise to quantization of energy level in form of Landau levels as illustrated in figure 1.4. If 'N' Landau levels are filled and the others are empty, then the unoccupied and occupied states are separated by an energy gap just like as an insulator. Contrary to an insulator, the Hall resistivity quantized as, $\rho_{xy} = h/Ne^2$, where h is Planck's constant, e is the electron charge and N is an integer. Interestingly, no symmetry breaking is needed to show this quantum phenomenon, which

classifies notable quantum phases of matter in condensed matter physics. The IQHE is a quantum mechanical aspect along with a topological one, which promoted the evolution of various quantum phases on the notion of topology.

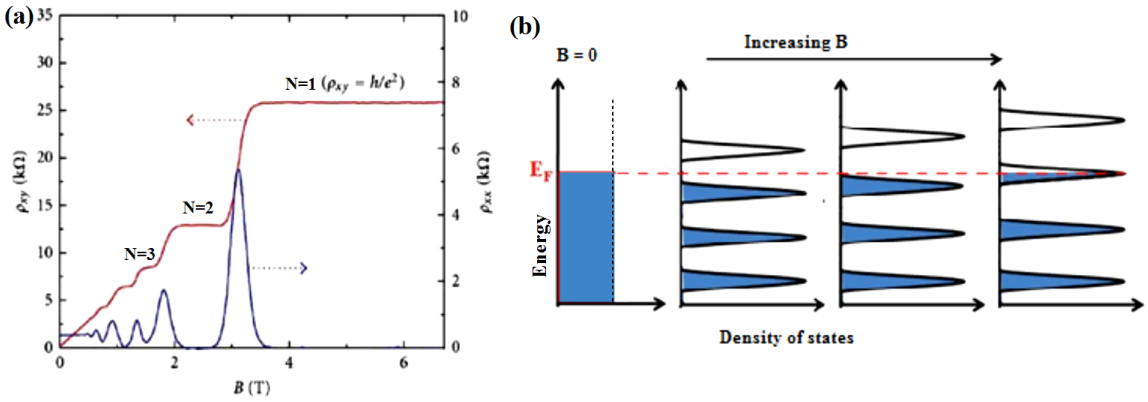

Figure 1.4: (a) Longitudinal (ρ_{xx}) and transverse resistivity (ρ_{xy}) variation with applied magnetic field revealing the integer quantum Hall Effect for InGaAs based heterostructure at a very low temperature. (b) Quantization of energy level in discrete Landau levels with application of magnetic field, by increasing of magnetic field strength, only those Landau levels that lie below the Fermi level (E_F) are occupied. (Adapted from [10])

An important feature of the IQHE state is the presence of edge states that arise due to incomplete cyclotron orbit at the edge of a 2DEG sample. Hence they form skipping orbits at the edge of 2DEG sample. However, inner electron states get quantized in cyclotron orbits as mentioned earlier.

The conduction along these edge states is unidirectional, according to the direction of applied external magnetic field on the system. This is a direct consequence of the topological character of gapped band structures. The electrons at one edge travel along one direction and the electrons on the other edge travel in the opposite direction in skipping orbits as shown in figure 1.5.

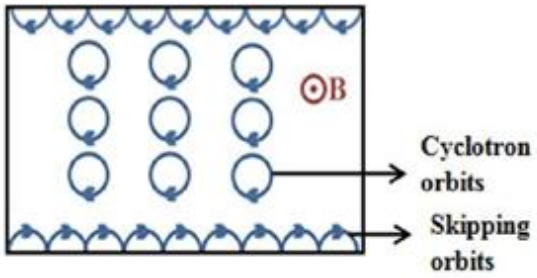

Figure 1.5: The integer quantum Hall state with skipping orbits forming the edge states.

1.5.3 Quantum Spin Hall Effect (QSHE)

The QSHE is the basic foundation of 2D topological insulator, which is equivalent to the two copies of the IQHE with two spin polarized edge states to maintain TRS, proposed by Kane & Mele in 2005 [11]. In QSHE, electrons with spin-down and spin-up move in opposite directions to form spin-polarized currents on the edge states due to the SOC even without application of any external magnetic field, as illustrated in figure 1.6. (b). The SOC lifts the spin degeneracy of the edge states, resulting in the chiral states at each edge of the sample that correspond to the two spins of the electron.

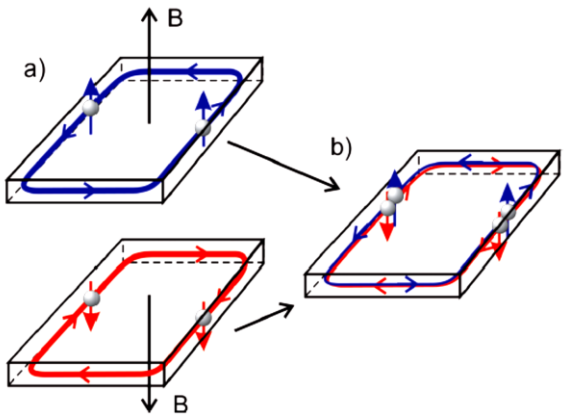

Figure 1.6: (a) Two copies of a QHE edge state for an opposite magnetic field. (b) An amalgamation of these two QHE states creates a quantum spin Hall state without a magnetic field. (Adapted from [12])

It can be noted that even two opposite channels are now present at the edge of the sample but backscattering is still not present because of the formation of the Kramer's doublets,

which protected by TRS. Therefore, when an up spin right-moving electron backscatters from a non-magnetic impurity, it undergoes a phase difference π in this process and turns to a left-moving down spin electron. Similarly a left-moving down spin electron becomes an up spin right-moving electron after backscattering. These two reflected wave functions interfere destructively and permit dissipation less transport.

In 2006, Bernevig, et al. [13] theoretically calculated that the quantum spin Hall phase may be observed in HgTe quantum wells. Soon after this prediction, in 2007 König et al. [14] experimentally observed QSHE in HgTe in zero magnetic field.

1.5.4 Anomalous Hall Effect (AHE) and Topological Hall Effect (THE)

Soon after the discovery of Hall effect in non-magnetic conductor under the applied magnetic field, in 1881, the Hall effect has also been observed in ferromagnetic ordered materials without any applied external magnetic field. This measured Hall effect in the zero magnetic field originated from the spontaneous magnetization of ferromagnetic materials, formally known as anomalous Hall effect (AHE).

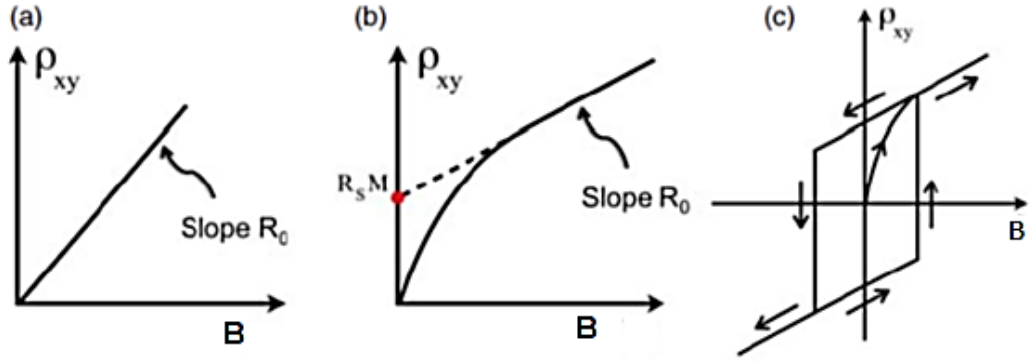

Figure 1.7: The variation of Hall resistivity ρ_{xy} with respect to external magnetic field B. (a) The ordinary Hall effect, (b) The contribution anomalous Hall effect (AHE) (c) The measured hysteresis loop from quantum anomalous Hall effect (QAHE). (Adapted from [15])

It is observed as an additional effect with ordinary Hall effect due to which a large slope in Hall resistivity at the low field was found as illustrated in figure 1.7.

This nonlinear nature of Hall resistivity (ρ_{xy}) is associated to the AHE, which is related to the magnetization of the materials ($\rho_{xy} = R_0B + R_SM$), Similar to the QHE, the quantized version of AHE is known as quantum anomalous Hall effect (QAHE) [16]. The understanding of QAHE is uniquely important for the evolvement of dissipation less spintronic devices.

Furthermore, the Topological Hall Effect (THE) was also observed in certain material with magnetic ordering [17]. The AHE occurs because of the magnetic interaction of conduction and localized electrons, while the THE is a distinctive feature of topologically nontrivial spin textures. Generally, THE is observed in ferromagnetic materials, but recently it has also been observed in antiferromagnetic systems [18]. The THE can be understood as, when an electron travels through a spatially varying magnetization of a 2DEG, if the magnetization is large enough, it will follow the local magnetization direction adiabatically.

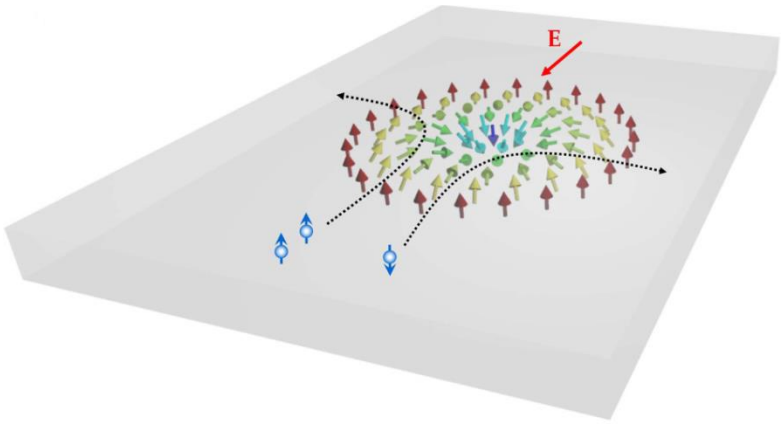

Figure 1.8: Schematics diagram of the THE due to scattering of spin-down and spin-up electrons from a Skyrmion binding in a ferromagnetic thin film with external applied electric field E. (Adapted from [19])

The electron in its own rest frame will experience a time-dependent magnetic field that will grab a Berry phase. The effect of this Berry phase can relate to an effective applied

magnetic flux perpendicular to the system. By this relation, the spatially changing magnetization and its related Berry phase is induced a Hall effect, which is known as THE. Basically, THE depends exclusively on the topology of the magnetic texture in the material. Hence, THE is observed in those topological materials, which have magnetic spin texture or presence of Skyrmion phase as shown in figure 1.8.

1.5.5 The Concept of Berry Phase

The fermions are spin polarized due the presence of SOC in the system which leads to π Berry phase which is the peculiar characteristic feature of QSHE states as we have discussed in previous section. Basically, the Berry phase is the phase difference that gained by a fermion wave function after completing a closed loop in a parametric space. We can understand it with the help of the schematic diagram which is illustrated in figure 1.9. Let us consider an electron performing a closed loop in real space with position vector **r** and momentum vector **k** as displaced in figure 1.9 (a). Let the behavior of electron is described by a wave function ψ. When an electric field **E** is applied, then the electron endures an effective magnetic field $\mathbf{B_{eff}}$, which interacts to its spin vector. This coupling then elevates the spin degeneracy of the spin states, due to elevation of this degeneracy, a Dirac cone is formed in the momentum space with two opposite chirality. These spins are revolving with one chirality at the one end of the Dirac Cone, and the opposite chirality at the other end of the Dirac cone as shown in figure 1.9 (b). However, in electron's rest frame, it experiences a rotating magnetic field which alters the Berry phase of the wave function as well as spin direction θ. For each and every closed cycle completed in real space, the value of θ sweeps to 2π, although, the Berry phase changes by π only. In consequence, the wave function ψ changes from ψ to $-\psi$. Therefore, to return to its original value of ψ in real space, the

electron must have to complete one more orbit i.e. two full orbits, as displayed in figure 1.9 (c) [20].

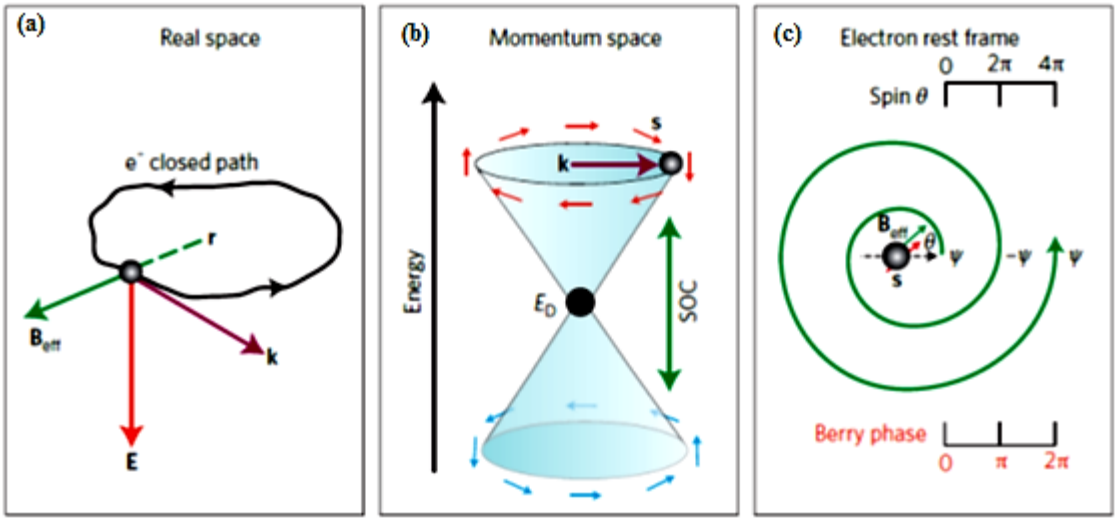

Figure 1.9: (a) The real space picture of electron's orbit (b) Formation of the Dirac cone due to SOC in momentum space (c) Berry phase and change in electron's wave function in its rest frame. (Adapted from [20])

1.5.6 Shubnikov-de Haas (SdH) Oscillations

The splitting of energy levels into discrete Landau levels in 2DEG subjected to a strong magnetic field perpendicular to its plane at low temperature has already discussed in previous section (1.5.2). Due to strong magnetic field, these electrons are localized in the plane of 2DEG and execute a cyclotron motion with the frequency $\omega_c = eB/m^*$, where e is the charge of electron, m* is the effective mass of the electron and B is applied magnetic field. Hence, energy of the discrete Landau levels can be expressed as,

$$E_N = \left(N + \frac{1}{2}\right)\hbar\omega_c \tag{1.3}$$

When the Landau level passes over the Fermi level as a consequence of continuous increase in applied magnetic field, due to broadening of the Landau level the Fermi level stays inside the Landau level for a short time. Therefore, during this time electrons get

scattered in that Landau level due to availability of vacant states just above the Fermi level and completely filled states just below the Fermi level. If the Fermi level stands somewhere in between two Landau levels, there is no scattering of electron inside the Landau levels. Hence, the resistivity changes periodically with increase in the applied magnetic field. Consequently, we observed oscillations in the longitudinal resistivity (ρ_{xx}) (figure 1.4), these oscillations are known as Shubnikov-de Haas (SdH) oscillations, whereas, if the oscillations observed in magnetization vs magnetic field data, they are called de Haas–van Alphen (dHvA) oscillations. In practice, these oscillations can be analyzed either by taking the second derivative of resistivity ($\rho_{xx)}$ with respect to applied magnetic field or after deducting a smooth background from the measured longitudinal resistivity data.

In TIs, from SdH oscillation analysis, effective mass, carrier lifetime, Dingle temperature and quantum mobility can be determined as well as Fermi surface can be mapped. Onsager relation gives us the relationship between the frequency (F) of oscillation and the Fermi wave vector $\mathbf{k_F}$ as [21],

$$F = \frac{\hbar}{2e}\mathbf{k_F}^2 \tag{1.4}$$

From this relation Fermi wave vector can be evaluated. In addition, SdH oscillations are also provide the information about the Berry phase. The value of Berry phase in normal metals for quadratic energy dispersion is zero, while in Dirac materials the value of the Berry phase for linear energy dispersion is π. The Berry phase from these quantum oscillations can be extracted after plotting the Landau fan diagram with the help of following relation [22].

$$2\pi\left(\frac{F}{B} - \frac{1}{2} + \gamma\right) = (2N-1)\pi \tag{1.5}$$

Thus, the plot between inverse magnetic field B^{-1} and Landau level index N gives a straight line, the slop of the linear fit of this plot is correspond to the frequency of oscillation (F) and the intercept on the Landau level index (N) axis gives the value of γ. γ = 0, represents zero Berry phase, whereas γ = 0.5 represents π Berry Phase [22].

The quantum oscillations can be expressed by Lifshitz−Kosevich equation [21], which is give as

$$\Delta\rho_{xx} = A_0 R_T R_D R_S \cos\left\{2\pi\left(\frac{F}{B} - \frac{1}{2} + \gamma\right)\right\} \quad (1.6)$$

Where, A_0 is a constant, R_T is thermal damping factor, R_D is the dingle factor and R_S is spin depending factor.

1.5.7 Weak Localization (WL) and Weak Antilocalization (WAL) Effects

The WAL effect in magnetoconductance is associated to the TSS in TIs. It appears at very low temperature and small magnetic field when negative conductivity varies as a variation of applied magnetic field. It has been realized that large spin-orbit scattering in some materials could leads to a change in quantum interference from constructive to destructive. Subsequently, the WAL effect appears due to enhancement in negative conductivity. On the other hand, in the weak localization (WL) effect, electrons in conductors are localized due to constructive interference between two time-reversed paths of the electron wave functions, which enhance the probability of electrons localization and reduce their ability of current transport. Therefore, application of a magnetic field induces a positive magnetoconductance. In the 1980, Hikami, Larkin and Nagaoka (HLN) analyzed the WAL and WL effects for 2D systems with the help of equation given as [23]

$$\Delta\sigma = \sigma(B) - \sigma(0) = A\left[\psi\left(\frac{1}{2} + \frac{h}{8\pi eBl_{\varphi}^2}\right) - ln\left(\frac{h}{8\pi eBl_{\varphi}^2}\right)\right] \quad (1.7)$$

Where, $A = \frac{\alpha e^2}{\pi h}$ represents the number of conduction channels, ψ is digamma function and l_{φ} is the phase coherence length. Like many semiconductors, the l_{φ} in TIs can be order nanometers to micrometer at low temperature. When size of the sample is comparable with l_{φ}, the quantum interference becomes important in transport and enhances the backscattering between two time-reversed scattering paths as shown in the figure 1.10. In TIs, due to spin-momentum locking, the spin directions in these two paths are always opposite to each other. As already explained in section 1.5.5, π Berry phase is accumulated for a closed loop. Thus, these two paths acquire phases of +π/2 and –π/2 and the π Berry phase thus leads to destructive interference. The constant term α from the HLN equation is then used to detect the type of localization, i.e. for WAL α = -0.5 and for WL α = 1.

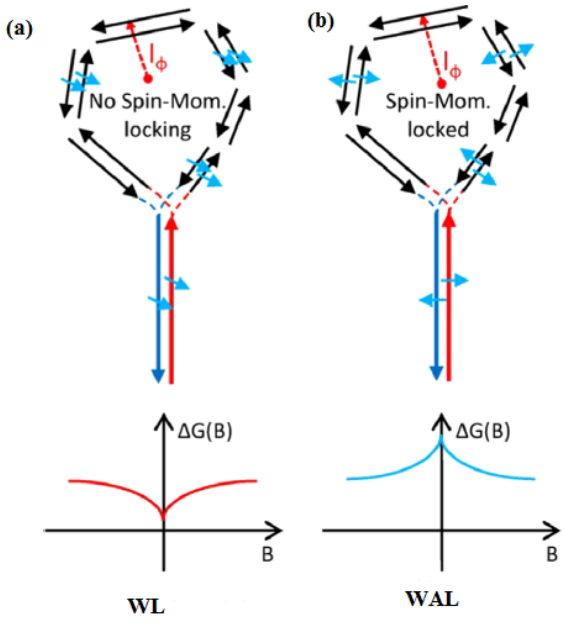

Figure 1.10: (a) The two time-reversed scattering loops without spin- momentum locking exhibiting weak localization in magnetoconductivity (ΔG (B)). (b) The two time-reversed scattering loops with spin- momentum locking exhibiting weak antilocalization in ΔG (B). (Adapted from [24])

1.5.8 Historical Developments of 2D and 3D Topological Insulators

As discussed in previous section 1.5.3 that electrons with dissimilar spins are move in opposite directions on the edge states to form spin-polarized currents due to the large SOC and preservation of TRS. In the beginning, Graphene was proposed to be the system that may show the QSHE, but because of weak SOC of carbon QSHE could not be observed in Graphene experimentally [11]. The presence of QSH state in HgTe quantum wells (QW) has been predicted by Bernevig et al. in 2006 [13]. A thin layer of HgTe inserted between two layers of CdTe to construct 2D QW structures that provide a special route to change the electronic structure of the compound. Soon after this theoretical envision, in 2007, König et al. [14] confirmed it experimentally by observing QSHE in HgTe at 30 mK in zero magnetic field. Therefore, HgTe QW is considered as the first 2D TI. After the experimental validation of QSHE in CdTe/HgTe/CdTe QW, it was also predicted that QSHE may also exist in type II semiconductor such as InAs/Gasb/AlSb, when Fermi level lies in the bulk band gap [25].

The idea of 2D systems may be continued to the 3D systems, with a condition that the system should has a strong SOC that generally presents in heavy elements. In 2007, Fu et al. predicted that $Bi_{1-x}Sb_x$ (x = 0.07-0.22) is a 3D TI based on electronic structure calculation and the connection between the presence of special conducting surface states and bulk topological order. A very next year after theoretical prediction, in 2008, Hsieh et al. [26] reported the discovery of the first 3D TI experimentally with the help angle-resolved photoemission spectroscopy (ARPES) by examining the energy dispersion of surface states. Dirac cone and TSS were experimentally observed in $Bi_{0.9}Sb_{0.1}$ using ARPES.

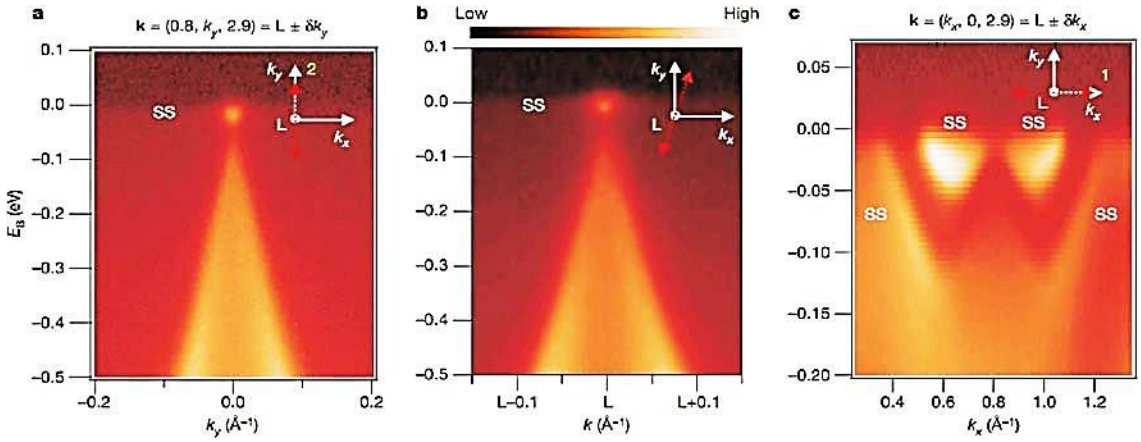

Figure 1.11: Selected three k-space cuts ARPES spectra of $Bi_{0.9}Sb_{0.1}$ (a) along k_y direction; (b) with approximately 10° from the direction of k_y; (c) the k_x direction through the L-point of the bulk 3D Brillouin zone. (Adapted from [26])

Figure 1.11 displays the ARPES data for k-space cuts along the various directions. However some in the $Bi_{1-x}Sb_x$ system shows inherent shortcomings such as the small Sb doping range ($0.07 < x < 0.22$) in which the material could be tuned as a TI, narrow band-gap (0.03 eV at $x = 0.18$) and the presence of multiple surface states have subsequently made the system least interesting from research point of view.

Shortly after the experimental discovery of $Bi_{1-x}Sb_x$ system as a first 3D TI, in 2009, based on ab-initio calculations, Bi_2Te_3, Bi_2Se_3, Sb_2Te_3 are certain compounds of the A_2B_3 chalcogenides family predicted to realize as 3D TI by Zhang et al. [6]. Calculated bulk band gap and non-trivial surface states for Bi_2Se_3, Bi_2Te_3 and Sb_2Te_3 can be seen in figure 1.12.

The experimental validation of calculated band structure was done by three different groups in same year after theoretical prediction by using ARPES. Y. Xia et al. [4] verified topological nature of Bi_2Se_3 with bulk band gap ~0.3 eV, Dirac Point (DP) and surface states in Bi_2Te_3 discovered by Chen et al. [27] with bulk band gap ~0.1 eV and in Sb_2Te_3 by Hsieh et al. [28] with bulk band gap ~0.26 eV as illustrated in figure 1.12. The DP was

predicted to stay in the bulk band gap for Bi_2Se_3 and near the bulk valence band for Bi_2Te_3 and Sb_2Te_3.

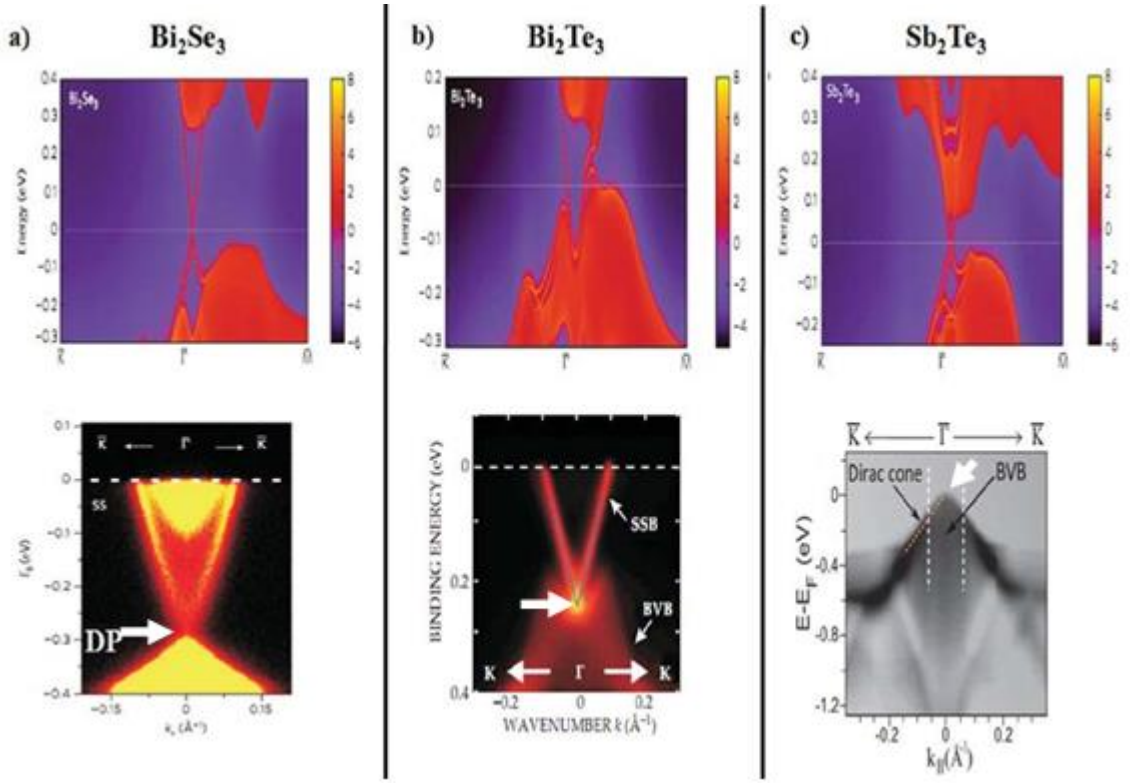

Figure 1.12: Theoretical calculated band structure [6] and ARPES data for (a) Bi_2Se_3 [4]; (b) Bi_2Te_3 [27] and (c) Sb_2Te_3 TIs [28].

Bi_2Se_3, Bi_2Te_3 and Sb_2Te_3 are the materials possess similar types of layered rhombohedral crystal structure with $R\bar{3}m$ space group. We have considered Bi_2Se_3 as an example; the structure consists five atoms in a unit cell arranged in Se1-Bi1-Se2-Bi1'-Se1' layered sequence along the 'c' axis known as quintuple layers. Each layer of atom forms a triangle lattice. For every layer, there are three possible sequential places A, B and C along the z direction. The triangle layers are arranged in the order A-B-C-A-B-C across the z-axis. The Se2 site acts as an inversion center, hence Bi1 is changed to Bi1' and Se1 is changed to Se1' under an inversion operation. The crystal structure of Bi_2Se_3 is shown in figure 1.13, where t_1, t_2 and t_3 are lattice primitive vectors of rhombohedral unit cell.

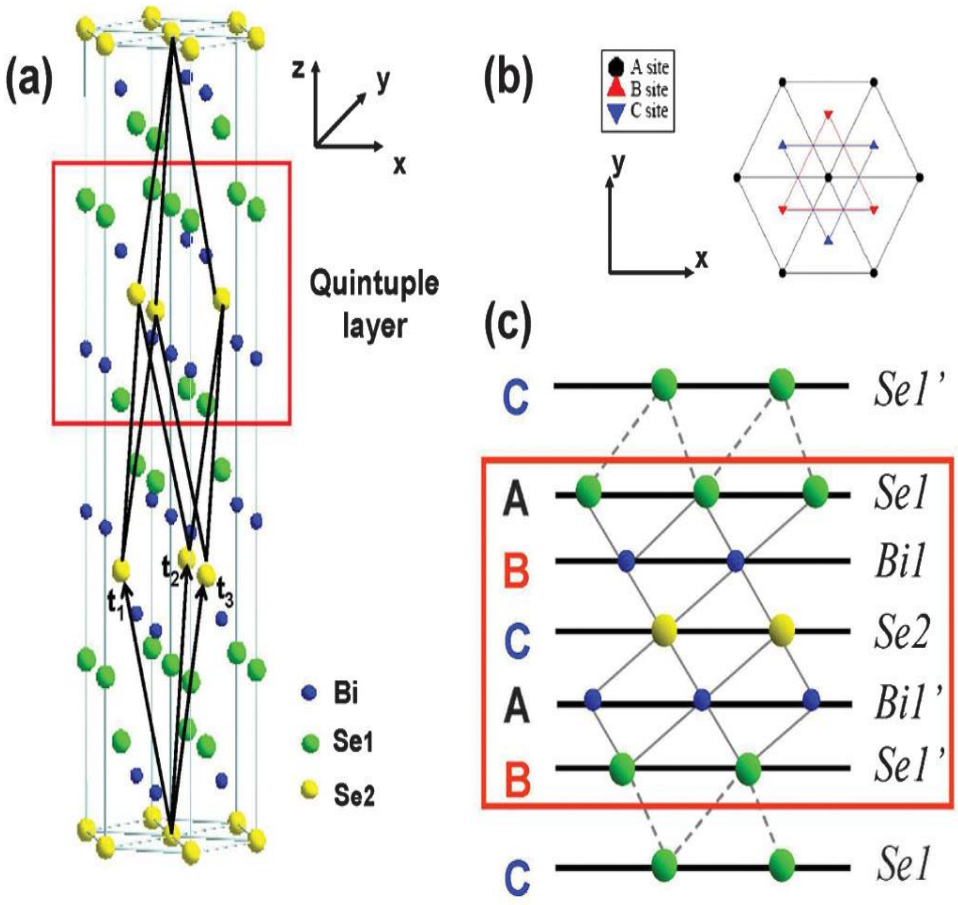

Figure 1.13: (a) Crystal structure of Bi_2Se_3, the red box shows single quintuple layer (b) shows that three different A, B, and C sites are assigned to triangular lattice in one quintuple layer (c) Se and Bi atoms are arranged in a sequence in quintuple layer. (Adapted from [6])

The strong SOC drives a band inversion at the Γ point in the Brillouin zone. figure 1.14 displays the schematic change in the atomic energy levels of Bi_2Se_3 and the effect of crystal field splitting and SOC on the energy eigenvalues at the Γ-point as calculated by Zhang et al. [6]. The outermost configuration of Bi and Se atoms are $6S^2$ $6p^3$ and $4S^2$ $4p^4$ respectively. Since a unit cell consists two Bi and three Se, and the outermost cell of each atoms contain three p-orbitals p_x, p_y and p_z, so there are total fifteen p-orbitals in a unit cell of Bi_2Se_3. In stage I, Bi energy levels are pushed up and Se levels are pushed down because of chemical bonding. In stage II, due to crystal field splitting Bi energy level splits in to two

levels with different parity i.e. one odd, one even denoted as $P1^{-}_{xyz}$, $P1^{+}_{xyz}$, respectively, whereas Se energy levels split in to three states with different parity i.e. two odd, one even denoted as $P0^{-}_{xyz}$, $P2^{-}_{xyz}$ and $P2^{+}_{xyz}$ respectively. In stage III, after taken SOC into consideration the energy level which is below the E_F moves to upside and the level which is above the E_F moves downward. Therefore, Strong SOC leads to band inversion in Bi_2Se_3 system.

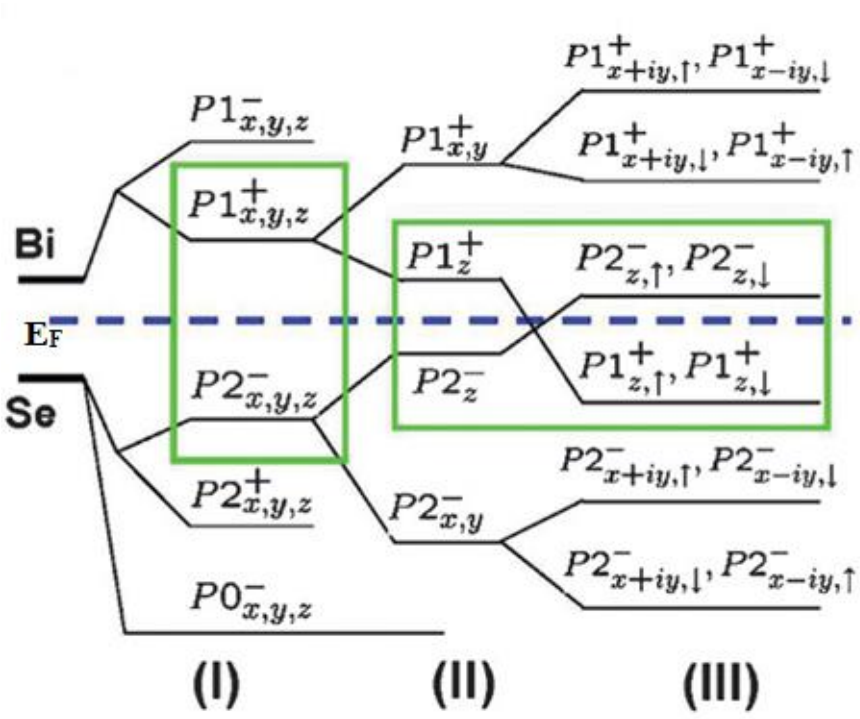

Figure 1.14: Schematic picture of the band inversion of Bi and Se p-orbitals in Bi_2Se_3 at the r-point. Stage I represents the effect of chemical bonding, Stage II represents the crystal field splitting, Stage III represents the effect of SOC. (Adapted from [6])

When a magnetic impurity is doped in a TI then unusual magnetotransport effects are noticed in these magnetically doped TIs due to broken of TRS. Various 3d-transition metal elements doped magnetic TIs have been investigated theoretically and experimentally [29], [30]. Mn doped Bi_2Te_3 [31] clearly exhibited the ferromagnetic ordering at 12 K for doping concentration up to 9%. On the other hand, Fe and Mn doped Bi_2Se_3 do not show the

ferromagnetic ordering, however a small surface state gap opened at the DP as confirmed from the ARPES measurement [30]. Therefore, it is necessary to investigate various magnetic topological insulators for better understanding and technological applications.

Moreover, superconductivity can also be induced in TIs by creating either internal chemical pressure on doping or by applying external pressure. However, only few topological superconductor systems have been discovered so far. Cu-intercalated Bi_2Se_3 is an example of internal chemical pressure induced topological superconductor systems [32]. Whereas, The external pressure induced superconductivity has been observed in pure Bi_2Te_3 with T_c of ~3 K when external pressure applied in between 3 to 6 GPa [33].

1.6 Weyl Semimetal (WSM)

WSM is a topological phase of matter regarded as an intermediate state between metal and insulator, which can be considered as 3D analogous of Graphene by breaking either TRS or inversion symmetry (IS). In WSM, the valence band and conduction band touches each other in the bulk at certain points, these linear-dispersive band-crossing points in bulk are called Weyl nodes. Weyl nodes act as a magnetic monopole in momentum space and always produce in pairs. The charge of Weyl node is associated to the Berry flux in the momentum space. It has been manifested that the charge associated to Berry curvature in a band structure must be zero, hence total number of Weyl nodes must be even. The projection of the Weyl nodes on the surface Brillouin zone is connected by an open line surface states called Fermi arc [34], [35]. The low-energy bulk excitations of Weyl semimetal are Weyl fermions. The transport by such types of excitations in the materials is fascinating due to its unique properties and potential applications.

The Weyl fermion was first introduced by Hermann Weyl in 1929 [36], one year after Dirac introduced equation for relativistic particles [37]. Dirac solved the Schrodinger equation for relativistic particles and depicted free electrons and positrons. A Dirac fermion is an outcome of the Dirac equation $H\psi = E\psi$ with Dirac Hamiltonian,

$$H = p_x\alpha_x + p_y\alpha_y + p_z\alpha_z + m\beta \tag{1.8}$$

Where, p_x, p_y and p_z are three momentum components, m is the mass of the fermion and $\alpha_x, \alpha_y, \alpha_z$ and β are anticommuting 4×4 matrices with $\beta^2 = 1$. If we considered above Hamiltonian in solids, one would have energy band as

$$E = \pm\sqrt{p_x^2 + p_y^2 + p_z^2 + m^2} \tag{1.9}$$

The mass term m will play the role of an energy gap in the band structure as shown in figure 1.15.

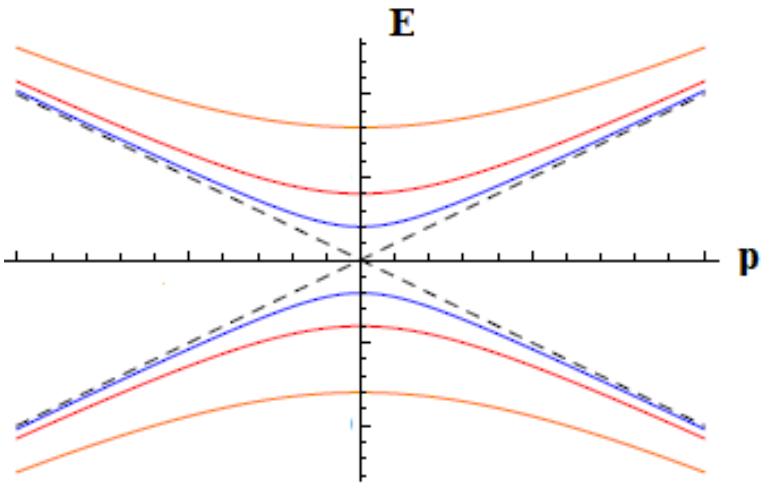

Figure 1.15: Energy with respect to momentum for different values of m (energy gap).The black dashed linear line is for m = 0 with zero energy. If $m \neq 0$, the energy gap = 2m between positive and negative energy bands.

Hermann Weyl solved the Schrodinger equation for relativistic particles by considering if the particles are massless. At present, these massless fermions are known as Weyl fermions which can be described by a two component matrices instead of four component Dirac matrices. They are the outcome of Weyl equation $H\psi = E\psi$ with following Weyl Hamiltonian and energy,

$$H = p_x\sigma_x + p_y\sigma_y + p_z\sigma_z \tag{1.10}$$

$$E = \pm\sqrt{p_x^2 + p_y^2 + p_z^2} \tag{1.11}$$

Where, σ_x, σ_y and σ_z are 2×2 Pauli matrices. Since σ_x, σ_y and σ_z are already coupled to p_x, p_y and p_z respectively, so there is no room for mass term. This means that a gap cannot be open; hence the bands touching points are stable. Such a 3D phase of matter which has the linear energy dispersion and certain gapless points in bulk is conventionally called WSM.

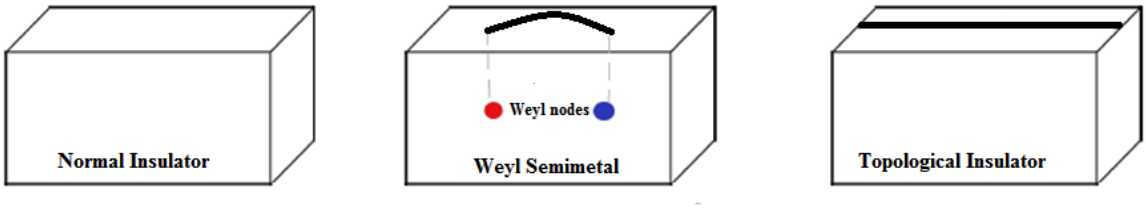

Figure 1.16: Schematics diagram of WSM phase, a phases between normal insulator and topological insulator.

It could be suitable to introduce Weyl semimetals in the context of topological phases. Unlike to normal insulators, topological insulators are insulator in their bulk but conductive at the surface of the material. In band structure terminology this means that there is a gap inside the material and gapless modes on its surface. Therefore, a natural question can be asked within this framework, is whether there are topological gapless phases with gapless edge states? We can say yes, WSM are believed to be a 3D realization of this kind of phase,

which allows the propagation of electron waves that behave as Weyl quasiparticles in the bulk at Weyl nodes and have arc like surface states on surface Brillouin zone which connects surface projection of Weyl nodes as illustrated in figure 1.16.

1.6.1 Helicity / Chirality

The massless particles are characterized by one important quantity known as Helicity. It is determined as projection of spin vector (**s**) on particle momentum direction. This is given as

$$\chi = \frac{p.s}{|p||s|} \tag{1.12}$$

Where $\mathbf{s} = \hbar\boldsymbol{\sigma}/2$ and χ is the helicity operator. The helicity operator has the eigenvalues ± 1, if spin vector aligned along the momentum direction then the eigenvalue of helicity operator is +1 and if spin vector aligned opposite to the momentum direction then the eigenvalue is -1. This leads to a picture where a Weyl node resembles to a magnetic monopole in momentum space. The Weyl nodes with spin vectors oriented toward the momentum or in the opposite direction are shown in figure 1.17.

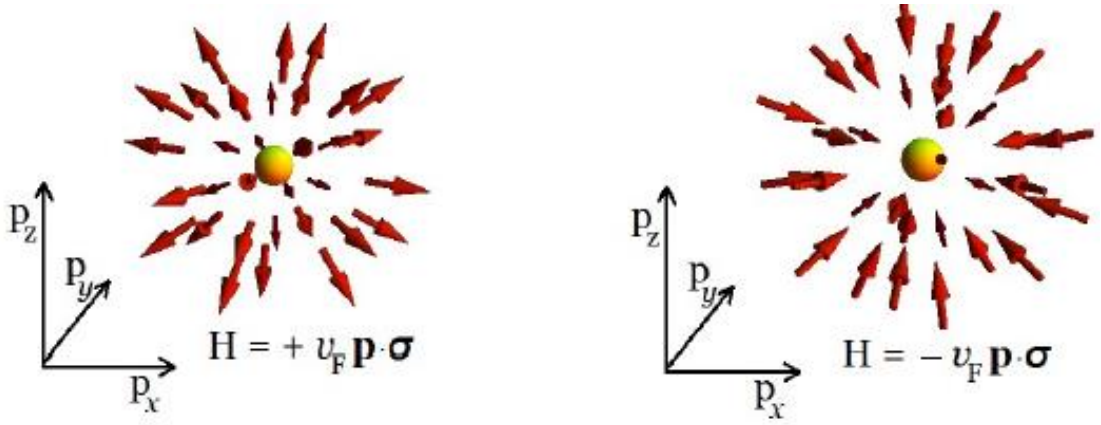

Figure 1.17: Pictorial view of Weyl nodes with opposite helicity.

1.6.2 The Role of Broken Symmetry

Breaking of symmetry is necessary for a transition from a Dirac semimetal to a WSM. Each Dirac node divides into two isolated Weyl nodes upon breaking of TRS with opposite momenta $\pm k_0$ and opposite chirality. Because preservation of IS needs Weyl points at opposite momentum -k and k that must carry opposite topological charge.

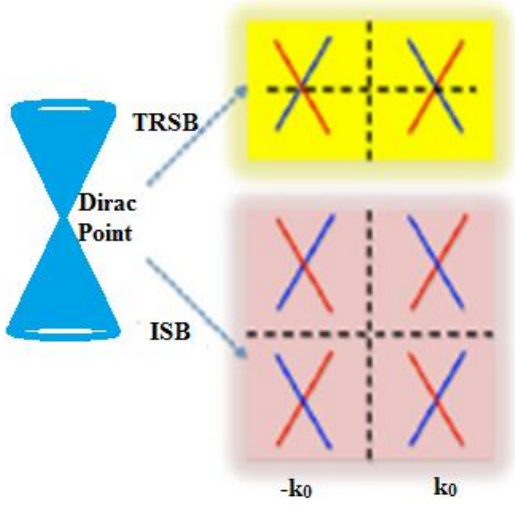

Figure 1.18: Schematics of Dirac point splitting into separated Weyl points upon breaking TRS and IS.

The breaking of IS enforces individual Dirac node to break into two pairs of isolated Weyl nodes at momentum $\pm k_0$ with same chirality. This arises because, if a Weyl node comes at a momentum k, then another Weyl node must come at opposite momentum -k with identical topological charge to preserve TRS. Because, overall topological charge linked to the entire Fermi surface must be zero. Hence, there must be two more Weyl nodes of opposite topological charge at $-k_0$ and k_0 as shown in figure 1.18. Breaking both TRS and IS creates Weyl nodes at any k with different energies which is hard to probe experimentally.

1.6.3 Type I and Type II WSMs

WSMs have been classified into two category, type I and type II, those respect Lorentz symmetry and possess point like Fermi surface at Weyl point are categorized as type I WSMs. While those do not respect Lorentz symmetry and Fermi surface lies at the boundary between electron and hole pockets are categorized as type II WSMs as illustrated in figure 1.19.

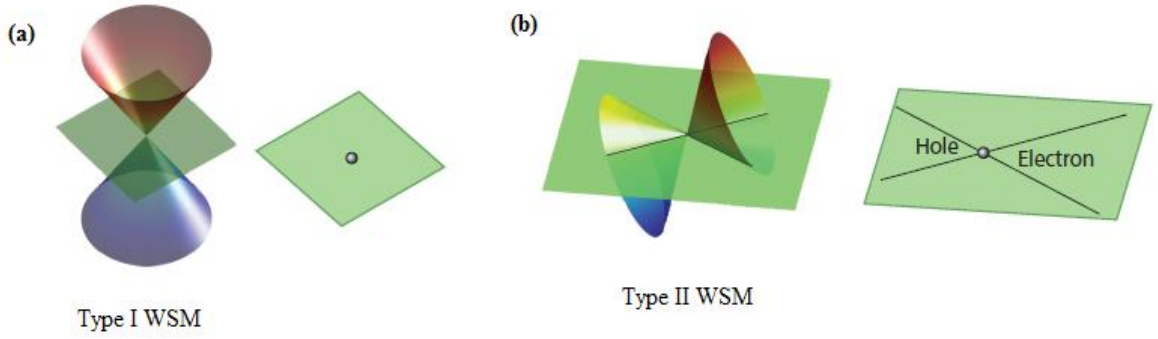

Figure 1.19: Weyl cone in **(a)** Type I WSM **(b)** Type II WSM. (Adapted from [34])

TaAs and NbP families evince ideal Weyl cones and fit in type-I WSM category [34]. $MoTe_2$ [38] and its sister compound WTe_2 [39] exhibits tilted Weyl cone so electron pocket and hole pocket touches at Fermi level. Hence, those WSMs are the member of Type-II category and they are anticipated to manifest different features from type-I WSMs.

1.6.4 Motion of Electron Inside These Exotic Materials (WSMs)

Researchers at Princeton University have noticed an odd behavior of electrons during the study of TaAs WSM material and suggested that the surface moving electrons sink into the bulk when they acquire a certain momentum called the Weyl momentum and appears on the opposite surface. It is like an electron on the surface of the crystal, and it is moving on it, as it gets unique value of momentum equal to Weyl point, it will sink into the crystal

through these conducting channels (Weyl points) and will come out on the opposite surface. Weyl nodes can be considered as a portal where the electrons may leave from one surface and may appear on the other surface. As Weyl nodes are come in pairs, so that a leaving electron could revert back through their partner point as shown in figure 1.20.

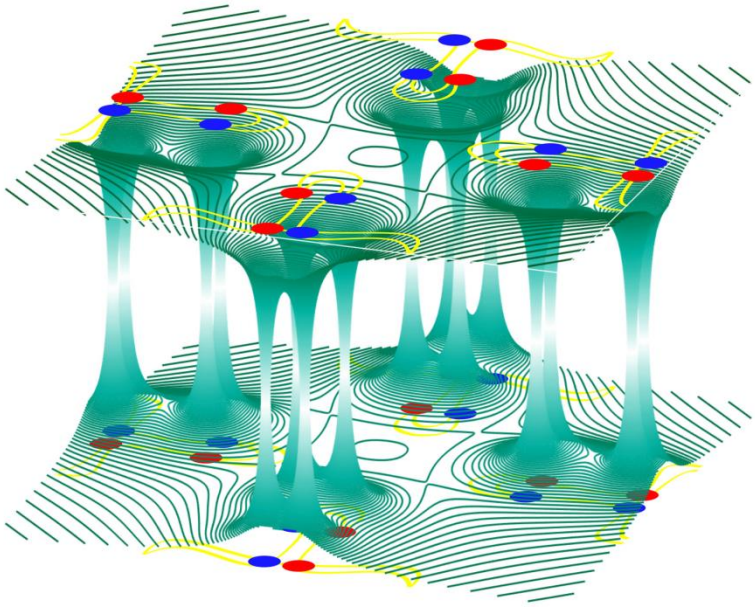

Figure 1.20: Schematic of connection between Weyl points (blue and red dots), special values of electron momentum, and Fermi arc (Yellow line) on the surface. (Adapted from https://blogs.princeton.edu/research/wpcontent/uploads/sites/56/2016/03/2016_03_10_Yazdani_Surface-bulk.jpg)

1.6.5 Experimental Actualization of WSMs

As discussed in previous section, either TRS or IS have to be broken in order to obtain a WSM state for experimental realization. TRS breaking can be acquired by magnetic doping. Therefore, the early assumptions to get WSMs were concentrated on magnetic materials, like $R_2Ir_2O_7$ and $HgCr_2Se_4$, which inherently breaks TRS. Although, because of the intricate magnetic domain structure of the samples, the experimental confirmation of these materials still remains a challenge [39]. Moreover, IS breaking phase of non-centrosymmetric transition metals such as TaAs, TaP NbAs and NbP has gained innumerable attention,

which have been propounded as promising WSM candidates. These compounds naturally break the IS because of their geometrical structure [40]. Hence, they are widely studied WSMs compounds. The surface Fermi arcs and bulk Weyl points predicted theoretically and observed experimentally by ARPES is shown in the figure 1.21, which assured topological nature of these WSM compounds.

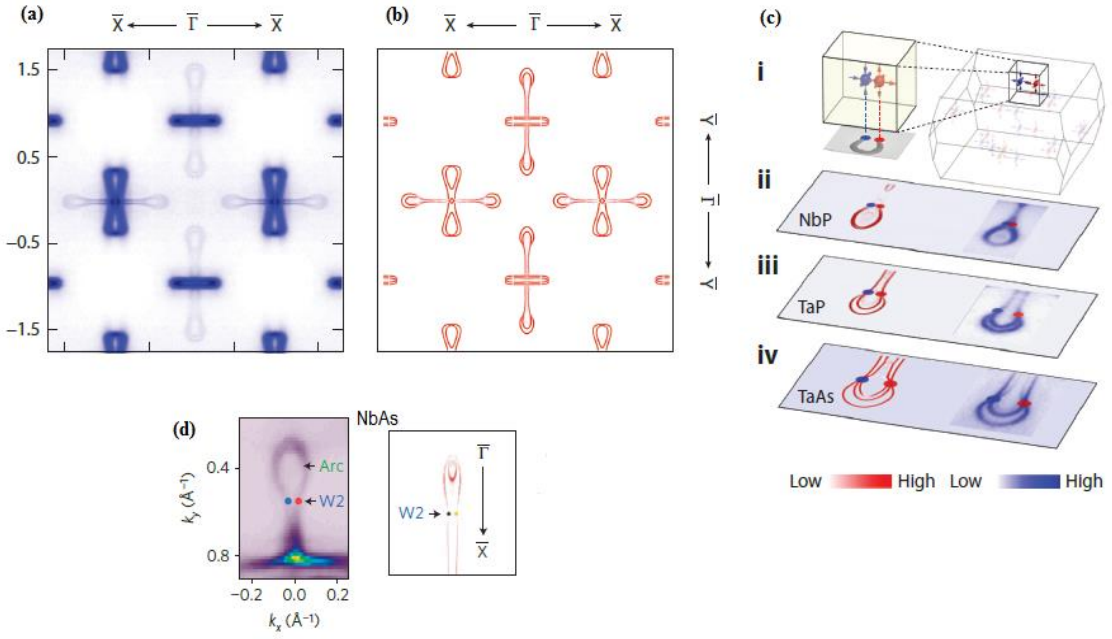

Figure 1.21: (a) ARPES measurement (b) Theoretical calculations of Fermi arcs and bulk Weyl points matched very well. (c) (i) Schematics of brillouin zone with Weyl nodes and Fermi arcs (ii) Comparison of Fermi arcs calculated theoretically and measured experimentally by ARPES for NbP, (iii) for TaP (iv) for TaAs. (d) for NbAs. (Adapted from [34], [41])

The 3D Fermi surfaces of WSMs family compounds have been reassembled by sensitive angle-dependent Shubnikov-de Haas (SdH) oscillations with theoretical band structure calculations. Very large magnetoresistance (MR) and ultrahigh carrier mobility has also been observed in these compounds as a consequence of electron-hole compensation. Hence, WSMs are the emerging materials over the last few years due to notable potential application in technologies.